Supplementary Information

Strain-Induced Metallization and Defect Suppression at Zipper-Like Interdigitated Atomically Thin Interfaces Enabling High-Efficiency Halide Perovskite Solar Cells

Nikolai Tsvetkov[1,†], Muhammad Ejaz Khan[2,3†], Byeong Cheul Moon[1], Yong-Hoon Kim[2,*], and Jeung Ku Kang[1,4*]

[1]*Department of Materials Science and Engineering, Korea Advanced Institute of Science and Technology (KAIST), 291 Daehak-ro, Yuseong-gu, Daejeon 34141, Republic of Korea*

[2]*School of Electrical Engineering, Korea Advanced Institute of Science and Technology (KAIST), 291 Daehak-ro, Yuseong-gu, Daejeon 34141, Republic of Korea*

[3]*Department of Computer Engineering, National University of Technology, Islamabad 44000, Pakistan*

[4]*Department of Chemistry, California Institute of Technology, 1200 East California Blvd., Pasadena, California 91125, USA*

Section S1. Method details

Chemicals. All reagents, unless otherwise stated, were obtained from commercial sources (TCI Chemicals, Junsei, Sigma-Aldrich, Lumtec corp., and Duksan and were used without purification. Specifically, PbI_2, MABr, $PbCl_2$, and FAI powders were purchased from TCI Chemicals. Titanium tetrachloride and lead chloride were purchased from Junsei. Chlorobenzene, DMF and DMSO were purchased from Sigma-Aldrich. The Spiro-MeOTAD powder was purchased from Lumtec corp. Acetone, ethanol, and distilled water were purchased from Duksan.

Synthesis of samples. The FTO-etched glasses have been cleaned sequentially with DI water, ethanol and acetone for 15 minutes by using the ultrasonic bath. Substrates were treated using the UV-ozone plasma during 20 minutes. The TiO_2 blocking layer was deposited by spin-coating at velocity of 2000 rpm for 60 second using 0.3 M titanium diisopropoxide bis(acetylacetonate) in 1-butanol solution that was heated afterward at 125 °C for 5 minutes. Then, the substrates were annealed at 450 °C for 30 minutes. We also used spray pyrolysis as an alternative method to deposit the compact TiO_2 blocking layer. Then, the TiO_2 paste in ethanol (2:9 weight ratio) solution was spin-coated onto the substrate at 4000 rpm for 60 seconds and annealed at 125 °C for 5 minutes. Subsequently, the substrates were annealed at 450 °C for 30 minutes followed by the treatment in 40 mM $TiCl_4$ aqueous solution at 70 °C for 30 minutes. Next, substrates were washed using DI water and ethanol. Then, there were blow-dried with argon and annealed at 450 °C for 30 minutes. To deposit PbO, TiO_2 film layers were dipped into the aqueous $PbCl_2$ solution at 90 °C for 60 seconds and washed with water and ethanol. Next, the substrates were annealed at 450 °C for 30 minutes in air. The Pb contents on the surface of TiO_2 was controlled by changing the concentration of $PbCl_2$ solution varied from 2 mg/L to 12 mg/L. Also, the perovskite deposition was conducted inside the nitrogen filled glovebox with a moisture level of 10-15 ppm. For devices with highest efficiency, we used the triple cation perovskite with a nominal composition of $Cs_{0.05}(FA_{0.85}MA_{0.15})_{0.95}Pb(I_{0.85}Br_{0.15})_3$. The 1.5 M perovskite solution was prepared by dissolving in DMF:DMSO mixture (4:1 v/v) with stoichiometric amount of FAI, MABr, PbI_2 and $PbBr_2$. All powder reagents were purchased from TCI chemicals (Japan) and used without further purification. Finally, the appropriate amount of 1.5M solution of CsI dissolved in DMSO was added to the perovskite solution. After overnight stirring, the solution was deposited on the TiO_2 layer by spin coating at 500 rpm for 10 sec and at 6000 rpm for 25 sec sequentially. Next, the 250 µl of chlorobenzene solution was dropped at the film surface. Then, the substrates were annealed at 100 °C for 25 minutes. As regards to a hole transporting material, the Spiro-MeOTAD solution was deposited by spin-coating at 4000 rpm for 30 seconds. The solution was prepared by dissolving 72.3 mg of Spiro-MeOTAD powder (Lumtec, Taiwan) into the mixed solution of 28.8 µl 4-tert-butyl pyridine, 17.7 µl stock solution with 52 mg of Li-TFSI in 100 µl acetonitrile, and 1 ml of chlorobenzene. Finally, the 50 nm-thick gold layer was deposited using the thermal evaporator for the back electrode of a photovoltaic solar cell with a deposition rate of 3-4 Å/s.

FE-TEM (Field emission-transmission electron microscopy). For the TEM analysis (Double CS-corrected Titan cubed G2 60-300, produced by FEI company), Pb-capped TiO_2 powders were sintered on the FTO glass and then scratched out and dissolved in ethanol following by treatment in ultrasonic bath for 60 min. The obtained solution was placed on a Cu mesh grid. An energy dispersive spectrometer (EDS) attached to the TEM was used to obtain the local elemental information and the elemental line profiles.

XPS (X-ray photoelectron spectroscopy). The CBM positions were analyzed with the XPS spectra obtained using a Sigma Probe from Thermo VG Scientific, which is equipped with a 350 W Al anode X-ray source along with a multi-anode, pulse counting, and hemispherical analyzer. The spectra were collected using an incident photon energy of 1486.6 eV and corrected for the detector's work function. Calibration of the spectra was performed by referring to the C 1s peak (C-C bond) at 285.0 eV. The VBM positions were estimated by extrapolation of the leading edge in valence band spectra. The XPS measurements were performed with the 90° take-off angle giving the ~6 nm probing depth (depth from where 90% of all signal is coming, 3x IMPF) in TiO_2. Instrumental resolution was 47 meV.

XRD (X-ray diffraction spectroscopy). The powder X-ray spectra were obtained using a SmartLab θ-2θ diffractometer in the reflectance Bragg-Brentano geometry using a Johansson-type Ge (111) monochromator with filtered Cu Kα1 radiation, 1200 W (40 kV, 30 mA) power and a high-speed 1D detector (D/teX Ultra). The films deposited on FTO substrate were held in a holder stage and scanned at a scan speed of 2 °/min in a continuous mode.

Raman spectroscopy. The defects or distortions in the samples were determined using a high-resolution dispersive Raman microscope (ARAMIS, HORIBA) equipped with an Ar ion CW Laser (514.5 nm).

Reflective Energy Electron Loss Spectroscopy (REELS). The REELS spectra were obtained using the Auger electron spectroscopy (AES; VG microlab 350 system). The 500 eV beam was used for excitation. The FWHM of the main reflection peak was below 3 eV.

Electrochemical Impedance Spectroscopy (EIS). The EIS measurements were performed under open circuit condition and 100 mW/cm^2 illumination in the frequency range 1 MHz-1 Hz with the IVIUM potentiometer, and the modulated voltage was 10 mV. Before measurements, the samples were stabilized at the measurement conditions for 10 seconds.

Time Resolved Photoluminescence Spectroscopy (TRPL). The TRPL measurements were conducted using the time-correlated single photon counting (TCSPC) method using a fluorescence lifetime spectrometer (FL920, Edinburgh Instruments). The samples configuration was FTO/c-TiO_2/mp-TiO_2/perovskite. The tri-exponential function was used for decay-fitting of the PL decay curve based on the following equation of

$$f(t) = \sum_i A_i \, exp\left({}^{-t}/_{\tau_i} \right) + B$$

where A_i is the decay amplitude, τ_i is the decay lifetime, B is the constant and i is the exponential constant used for the decay fitting of the PL decay. The fastest decay constant was attributed to electron injection process from perovskite to TiO_2.

Characterization of photovoltaic properties. The photovoltaic parameters of solar cell devices were measured by the solar simulator (Newport, Oriel) with the potentiometer (Compactstat, IVIUM). The devices were measured under ambient air using the aperture mask with the active area of 0.105 cm^2. The I-V curves were recorded with the scan rate of 0.02 mV/s.

Section S2. Supplementary figures

Atomistic models for planar and interdigitated $TiO_2(001)/MAPbI_3(001)$ interfaces and charge density difference and projected density of states analyses. The planar and Pb-interdigitated anatase $TiO_2(101)/MAPbI_3(110)$ interface atomic models employed for our density functional theory (DFT) simulations are shown in Figures S1 and S2. The perfectly interdigitated model was prepared by replacing all (100%) Ti atoms in the planar $TiO_2/MAPbI_3$ interface by Pb atoms. To address the interfacial layer thickness effects, we also prepared the 200% Pb-substituted model by padding the 100% $TiO_2/MAPbI_3$ model by additional TiO_2 layer. The layered projected density of states (DOS) on the $TiO_2(101)/MAPbI_3(110)$ interface models (Figs. S1 and S2) are explored to characterize the variations in the distribution of electronic states for the atoms present in different layers across the interface before and after introducing Pb-doping. The layered PDOS plots in Fig. S2 revealed that TiO_2 and $MAPbI_3$ regions for all the models remain semiconducting, while the interdigitated region acquires metallicity. In the 200% sample, bandgap opens again in the additional PbO_2 layer region, indicating that the metallicity is spatially restricted to the atomically thin interdigitated $TiO_2/MAPbI_3$ interfacial region.

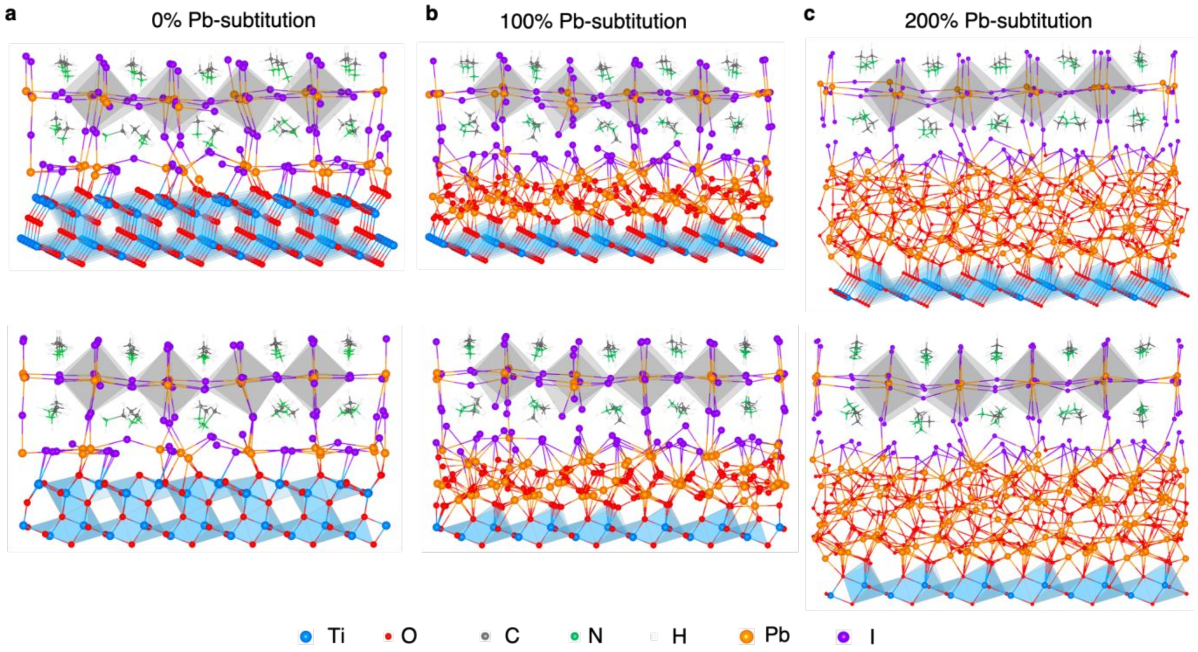

Figure S1. The TiO_2(101)/$MAPbI_3$(110) interface models optimized by DFT simulations shown in two viewing angles. (a) The planar interface, (b) the monolayer-level (100%) substitutionally Pb-doped interface, and (c) the bilayer-level (200 %) substitutionally Pb-doped interface models.

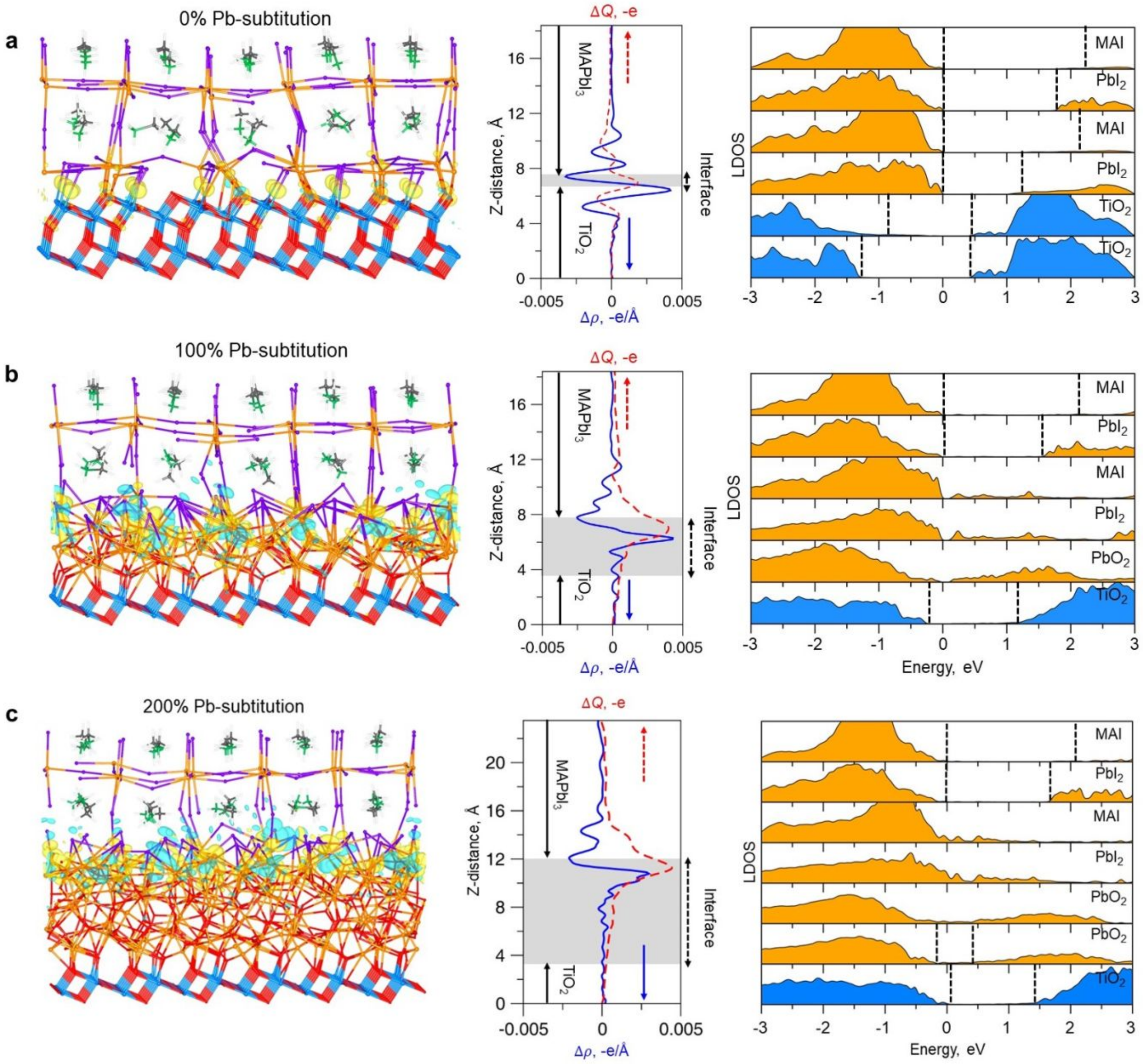

Figure S2. For the fully optimized (110)-MAPbI$_3$/(101)-TiO$_2$ interface models with (a) 0% (planar), (b) 100 % (one complete TiO$_2$ layer), and (c) 200 % (two complete TiO$_2$ layer) of interfacial Ti atoms substituted by Pb atoms (left panels), we calculated plane-averaged charge density differences (middle panel) and layer-by-layer projected DOS (right panels). In the structural models, the charge density differences are overlaid. Isosurface values are □0.005 eV/Å^3 and □0.005 eV/Å^3 for the charge accumulation (yellow) and depletion (cyan), respectively. The dotted lines in the layer-projected DOS plots indicate the valence and conduction band edges of semiconducting regions. For clarity, DOS of MA ligands are not included in projected DOS plots.

High resolution STEM characterization of TiO_2 nanoparticles with various PbO capping.

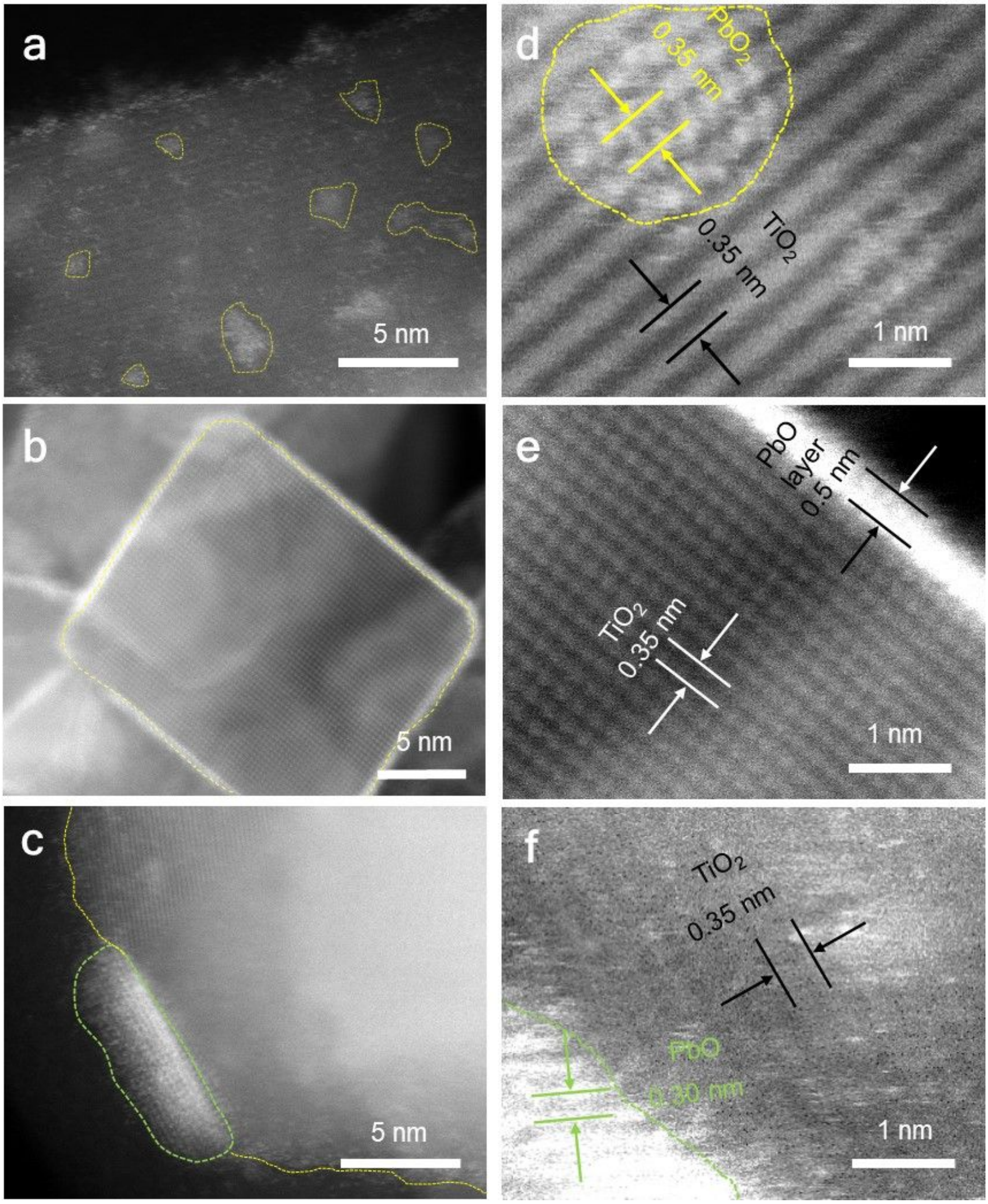

Figure S3. High resolution STEM images of (a) Pb7, (b) Pb13 and (c) Pb24 samples. Magnified images of the lattices for (d) Pb7, (e) Pb13, and (f) Pb24, where the more intense color corresponds to the stronger diffraction from heavy Pb atoms compared to lighter Ti atoms.

Experimental evidence of the absence of Cl atoms on Pb-capped TiO_2. XPS analysis shows the absence of the Cl atoms at the surface of Pb-capped TiO_2.

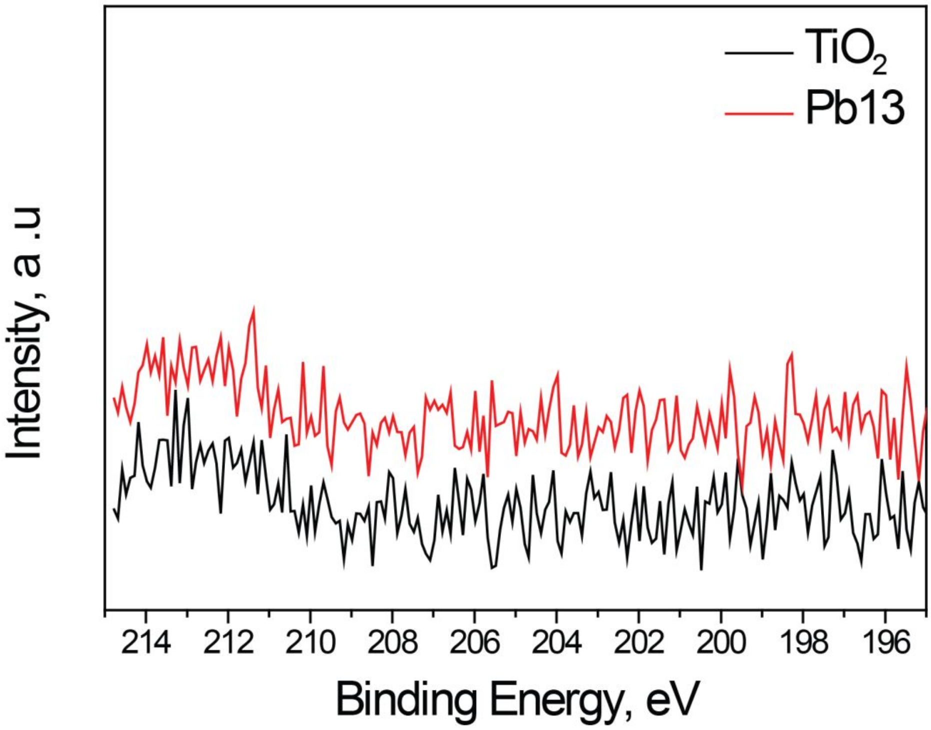

Figure S4. Cl 1s XPS core-level spectra of recorded from TiO_2 layers with (Pb13) and without Pb-capping.

Influence of PbO treatment on TiO_2 work function.

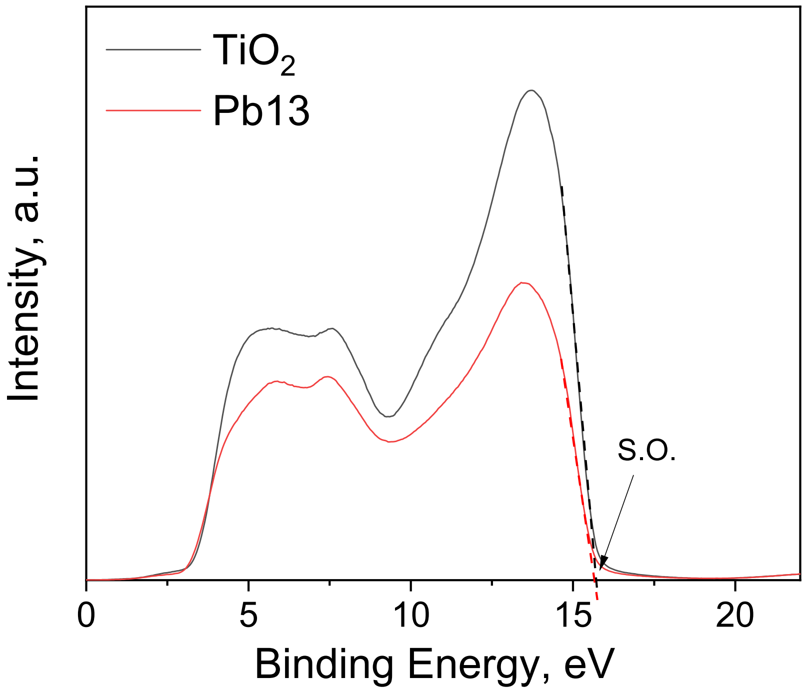

Figure S5. Ultraviolet photoelectron spectra of pristine and PbO-capped TiO_2.

Time-resolved photoluminescence measurements. The fastest component reflecting electron injection rate from $MAPbI_3$ to the ETL is shown to decrease from 8 ns to 4 ns as the bare TiO_2 is replaced by TiO_2 with PbO monolayer. However, for the Pb24-TiO_2 with an excessive amount of Pb atoms, the fastest component is increased up to 12 ns. Furthermore, we confirm that the Pb capping-induced 2D interfacial metallic states enhance the electron injection rate from $MAPbI_3$ to the Pb13-TiO_2. On the other hand, the slower electron injection is observed from $MAPbI_3$ to Pb24 with the formation of Pb^{3+} trap states within PbO clusters.

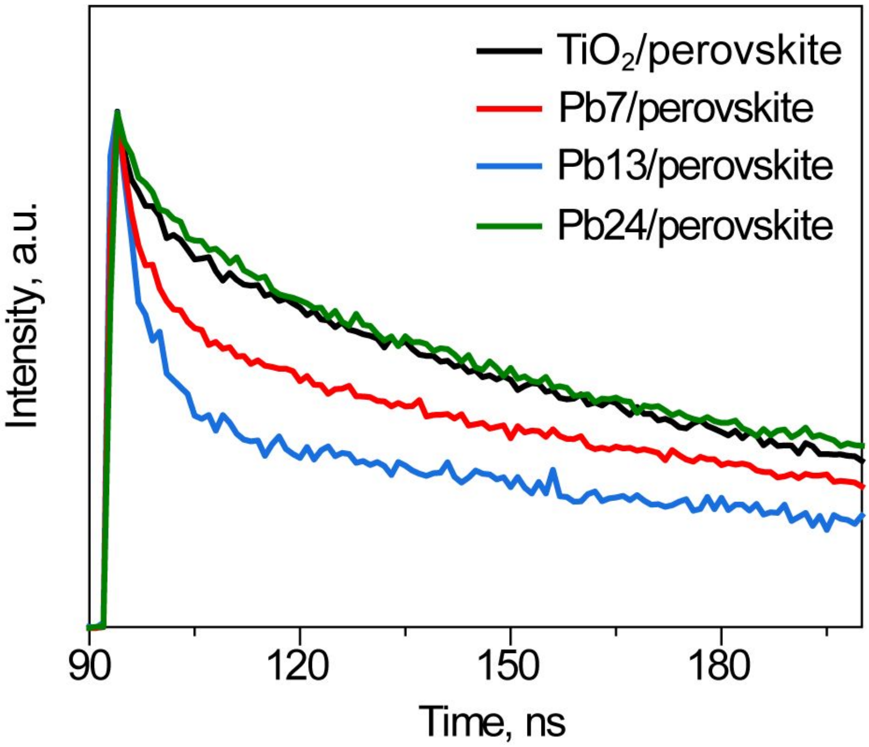

Figure S6. The TRPL decay curves of perovskite PL peak recorded from fluorine-doped tin oxide (FTO)/TiO_2/perovskite sample with bare and PbO-capped TiO_2 layers.

Crystal structure and morphology of perovskite deposited on TiO_2 ETL with and without PbO capping.

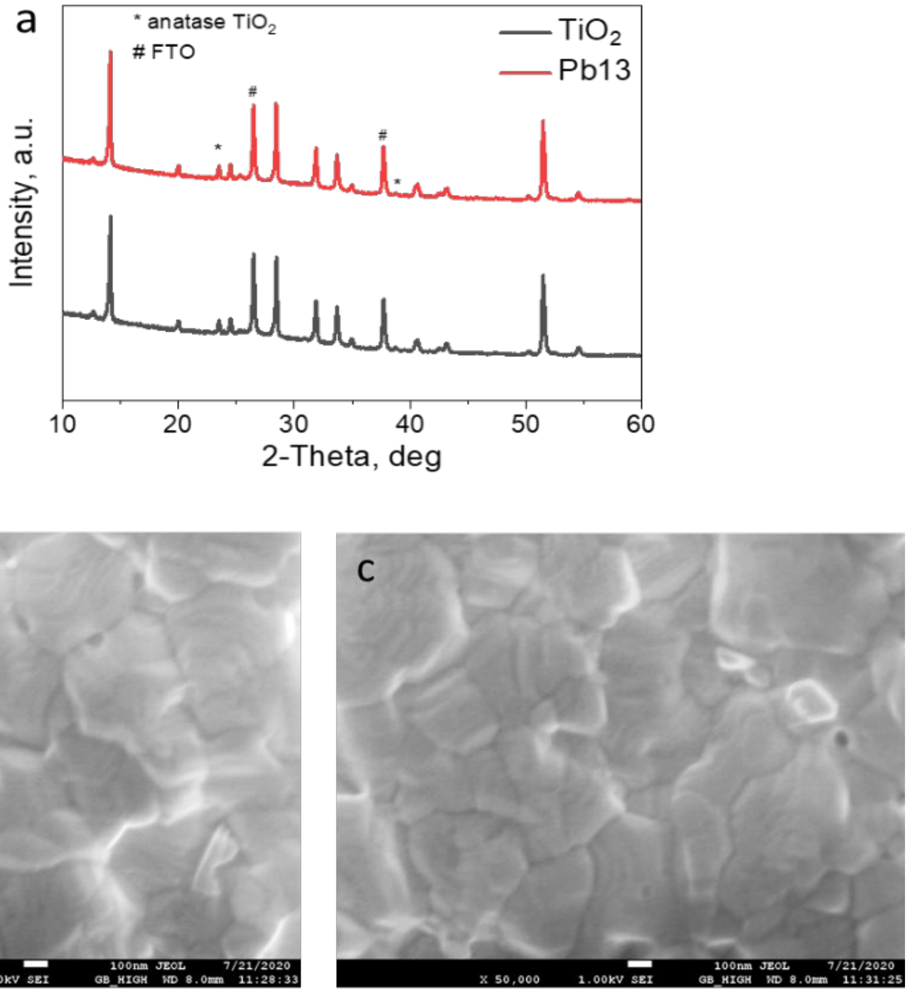

Figure S7. To check whether the perovskite grain size, morphology, and/or crystallinity (and thus the PSC perfomance) are not affected by the PbO capping of the TiO_2 subsrate, we compared the (a) XRD patterns and (b and c) SEM images of the perovskite layers grown on TiO_2 without and with PbO capping. They show negligible differences, so we attribute the observed differences in PSC performance to the change in the electronic structure at the perovskite-TiO_2 interface induced by the PbO capping of TiO_2.

Energy band alignment at the Pb-capped TiO_2 surface. The energy-dependent electronic structure of the non-Pb-capped and Pb-capped TiO_2 surfaces were investigated using XPS. The valence band spectra are shown in the Fig. S8 and the energy band diagram constructed using XPS and REELS results is depicted in Fig. S8d. Fig. S8a show the XPS measurement data of the Pb7, Pb13, and Pb24 TiO_2 ETL samples. They provide the information on the oxidation state of the Pb atom at the TiO_2 surface, which should influence the efficiency of charge transfer at the ETL/perovskite interface. The inorganic B-site cations such as Pb or Sn within halide perovskites are in the bivalent oxidation state (2+), and the higher oxidation-state sites at the interface can act as recombination centers, thereby playing to reduce the charge transfer efficiency. The main Pb $4f_{7/2}$ peaks from all the samples are located at around 139 eV, confirming that a Pb oxidation state is 2+. However, for the Pb24 structure, we find an extra shoulder in a lower binding energy region, which indicates the presence of Pb^{3+}. The partial trivalent oxidation state of Pb cations can be understood from the observation that Pb partially exists in the cluster form (Fig. S9), where Pb atoms are more oxidized compared to the bivalent state of Pb atoms incorporated into the TiO_2 lattice (Pb7 and Pb13 structures). Fig. S8b also shows the reflection electron energy loss spectroscopy (REELS) spectra used to explore the surface band gaps. For the TiO_2, Pb7, and Pb13 structures, we obtained the bandgap values of around 3.2 eV which is in a good agreement with that of the anatase TiO_2. However, for the Pb24 structure, the REELS spectra reveal a low-energy shoulder attributed to the smaller bandgap of PbO clusters, indicating that the conduction band of PbO clusters is located at around 0.5-0.7 eV below that of TiO_2 so that they can act as deep trap sites for electrons and decrease the charge transfer efficiency within ETL and/or across the ETL/perovskite interface.

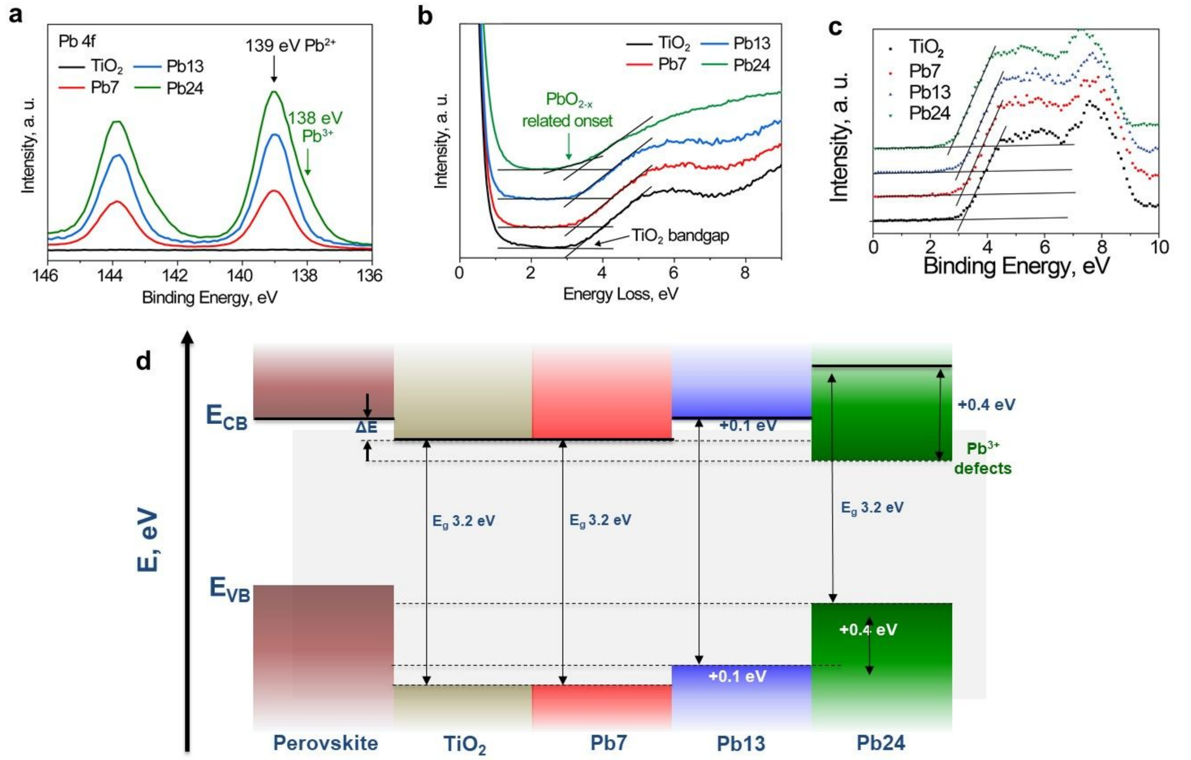

Figure S8. (a) The XPS spectra of Pb 4f peak recorded from TiO_2 with different Pb cappings. (b) REELS spectra of TiO_2 samples with different PbO cappings. (c) Valence band XPS spectra of TiO_2 with different Pb cappings**.** (d) Expected energy band alignment at the interface between $MAPbI_3$ and TiO_2 ETLs with different Pb cappings constructed based on XPS and REELS results. Note that here the possibility of forming metallic interfacial states is neglected.

XPS characterization of Pb-capped the TiO_2 nanoparticles with excess PbO coverage.

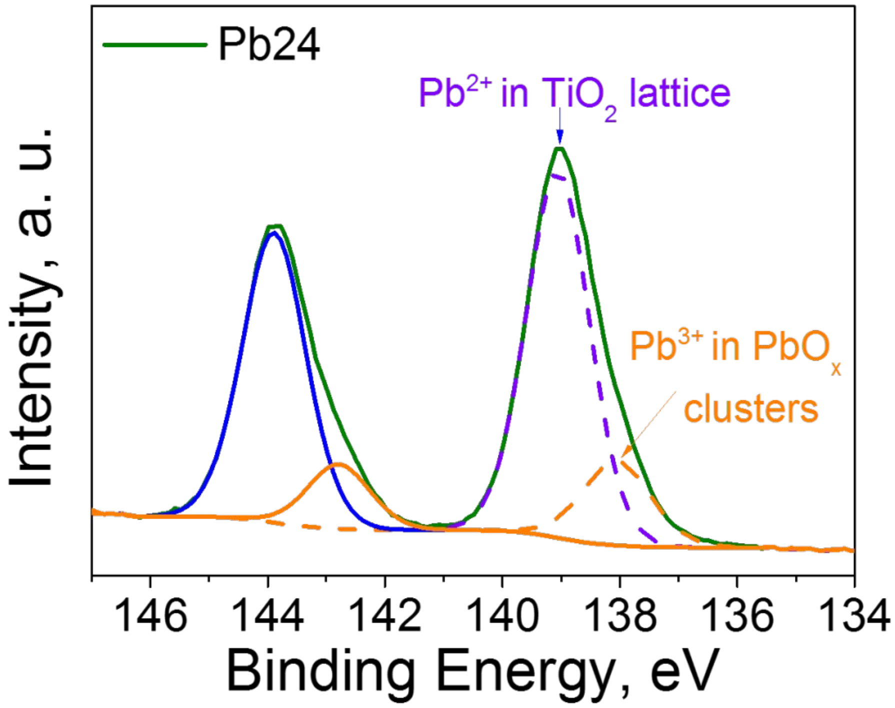

Figure S9. The deconvolutions of the Pb 4f XPS spectra for Pb24 sample showing the different Pb oxidation states.

FTIR characterization of the Pb-capped TiO_2. The FTIR transmittance spectra of mp-TiO_2 layers with different Pb capping are shown in Fig. S9. In the low wavelength part of spectra, no significant difference between different samples was observed. The difference was found only in long wavelength region. Especially, transmission drop (*i.e.* absorption peak) was detected at around 1350 cm^{-1} with the highest absorption for Pb13 and Pb24 samples. The low absorption in this are for Pb7 compared to Pb13 and Pb24 samples supports the hypothesis of incomplete PbO coverage for Pb7 samples. In addition, the special feature was observed in Pb24 samples at the shoulder of main peak, at around 1000 cm^{-1}. This feature was uniquely observed only for Pb24 sample and was attributed to presence of the special structure such as PbO clusters (Figs. S7 and S8).

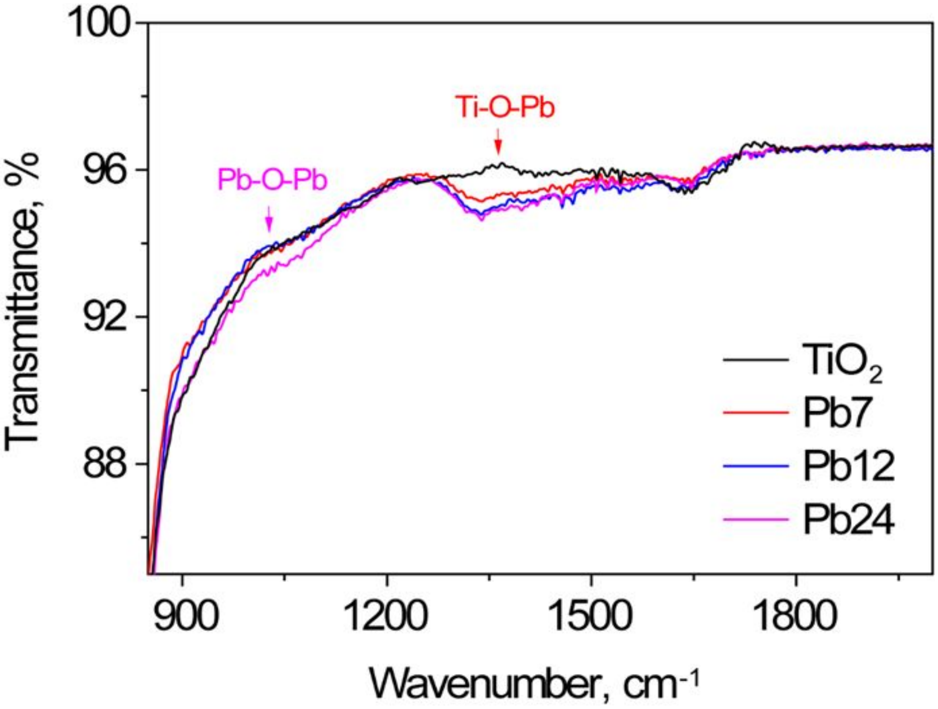

Figure S10. FTIR spectra of Pb-capped TiO_2 with different Pb loadings.

Bond length and interlayer spacing at the TiO_2/perovskite interfaces with and without PbO capping. The origin of emergent interfacial metallicity was verified based on the good agreement between the experimentally measured and theoretically calculated atomic bond-length and interlayer variations in the substitutionally Pb-doped TiO_2(101)/$MAPbI_3$(110) interface (Figures 3b and 3c), which is significantly different from those in its TiO_2(101)/$MAPbI_3$(110) counterpart (without PbO capping) shown below.

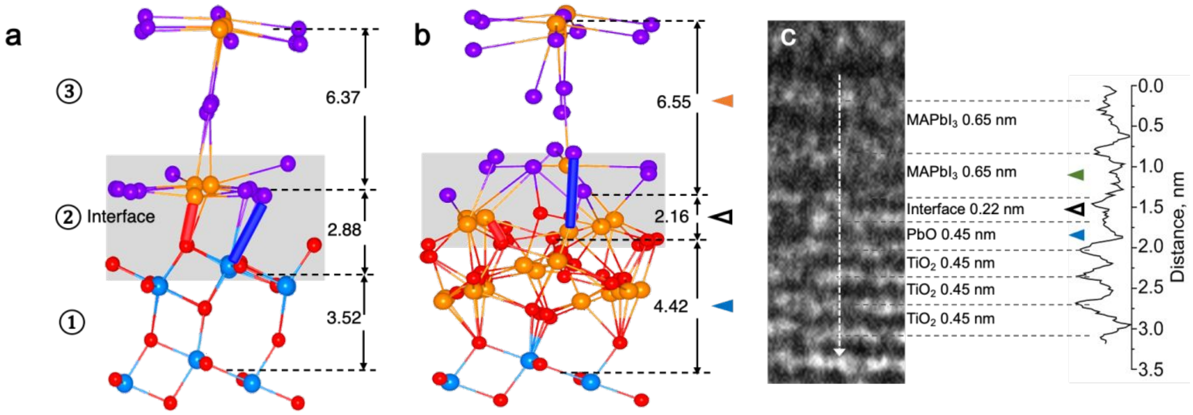

Figure S11. (a) The DFT-optimized atomic structure of the planar TiO_2(101)/$MAPbI_3$(110) interface. The (b) computationally and (c) experimentally obtained atomic structures for the Pb-interdigitated TiO_2(101)/$MAPbI_3$(110) interface are reproduced for comparison [Figure 2(c) and 2(b), respectively]. Note that interlayer spacing variations are notably different from the planar and interdigitated TiO_2(101)/$MAPbI_3$(110) models.

Chemical composition at the TiO_2/perovskite interface. After the perovskite deposition, the capping layer was scratched out and mp-TiO_2/perovskite layer was exposed to the X-ray beam for XPS measurements. On the survey scans, both Ti and Pb peaks are clearly visible, indicating that some parts of signals are coming from the interface between the mp-TiO_2 and the perovskite.

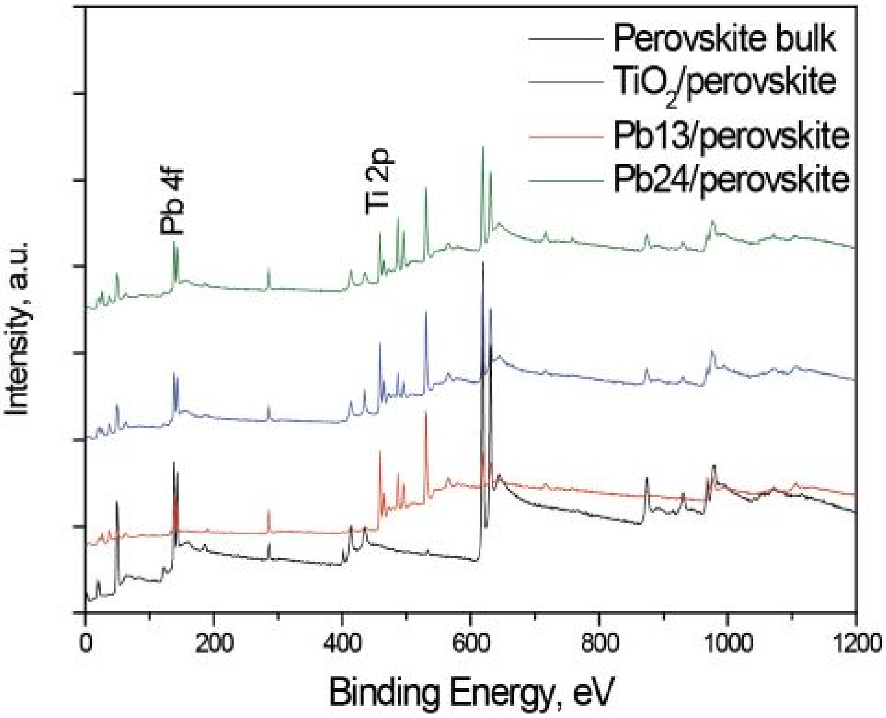

Figure S12. Chemical composition at TiO_2/perovskite interfaces. The XPS survey scans of interface between a perovskite and a Pb capped TiO_2. The survey scan of bulk perovskite was also given as a reference.

Current-voltage behaviors the TiO_2/perovskite interface.

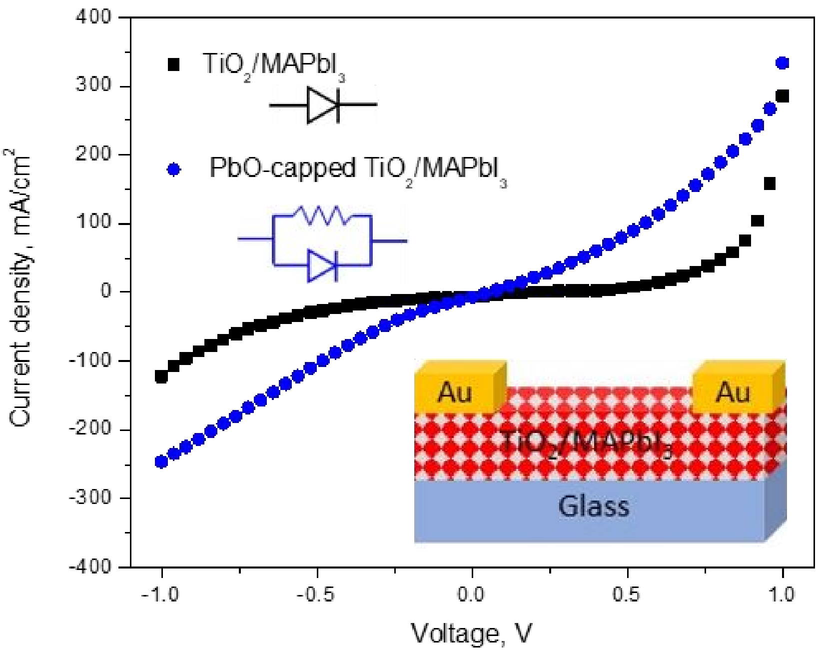

Figure S13. Current-voltage curves obtained from the in-plane measurements of the TiO_2/perovskite samples with and without PbO capping of TiO_2. While the TiO_2/perovskite interface without PbO capping exhibits a typical semiconducting behavior, the PbO-capped TiO_2/perovskite interface shows a linear Ohmic-like or metallic behavior, which we ascribe to the formation of metallic states at the interface. The sample configuration is given in the bottom right corner.

DFT analysis of defects at the TiO_2/perovskite interface.

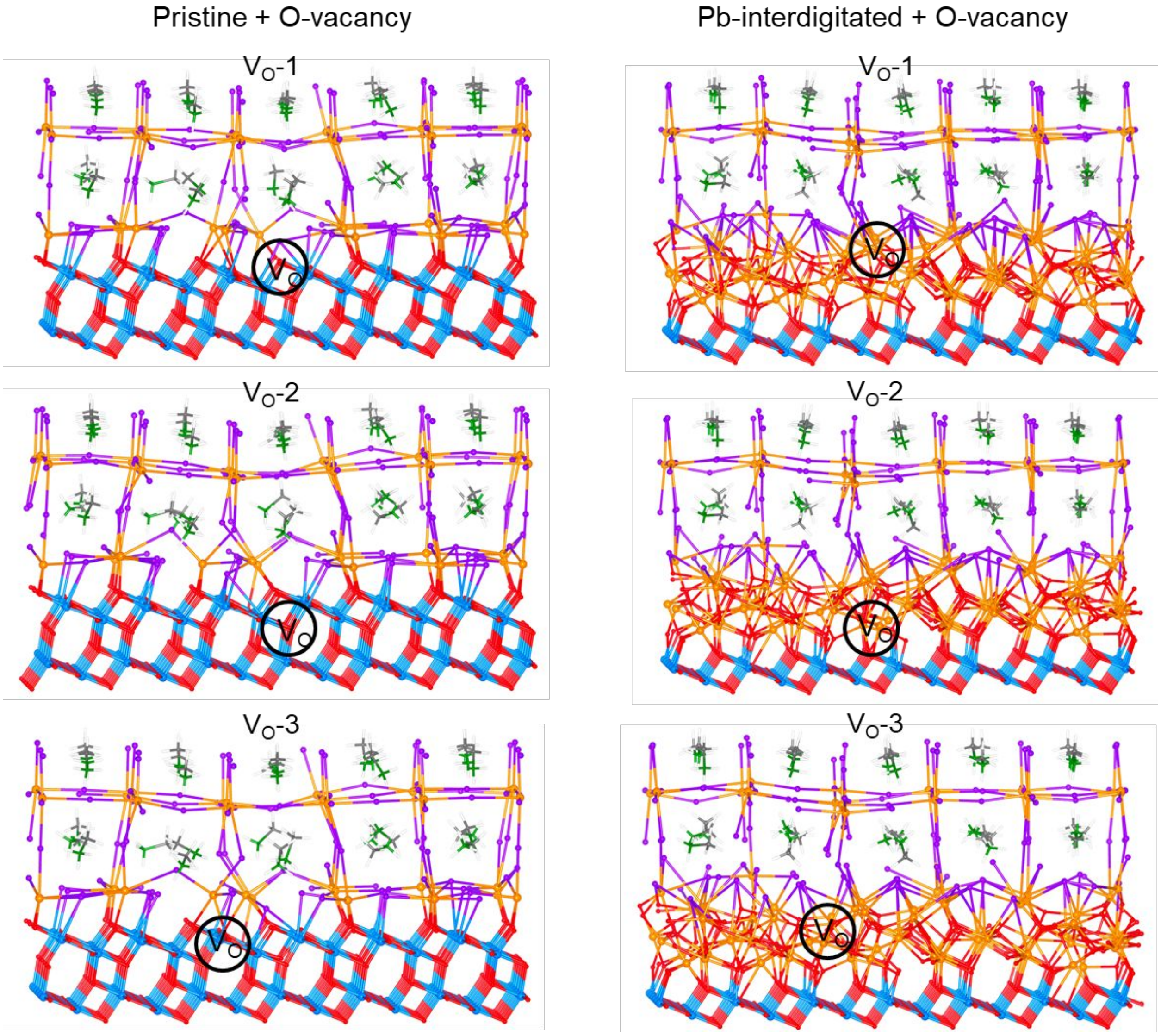

Figure S14. Atomic structures of the (left panels) planar and Pb-interdigitated (right panels) TiO_2/$MAPbI_3$ interface models with one oxygen vacancy defect incorporated at different sites, marked with solid a solid circle in each atomic model.

Layer-by-layer projected DOS calculated for the planar TiO_2/$MAPbI_3$ interface.

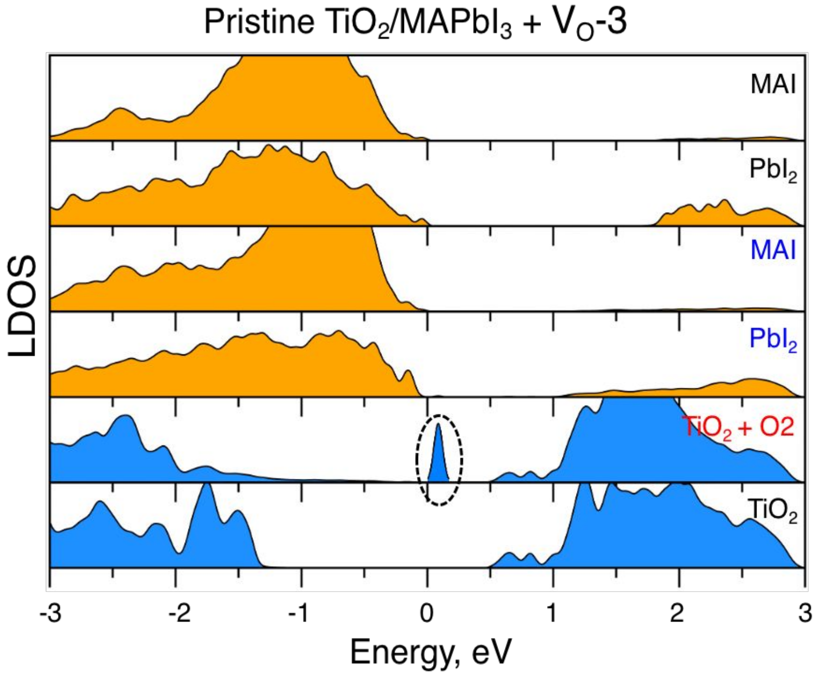

Figure S15. Layer-by-layer projected DOS calculated for the planar TiO_2/$MAPbI_3$ interface with one oxygen vacancy incorporated at the TiO_2 surface layer. The dashed ellipsoid marks the deep defect levels generated by the oxygen vacancy.

Hysteresis behavior and performance of PSCs.

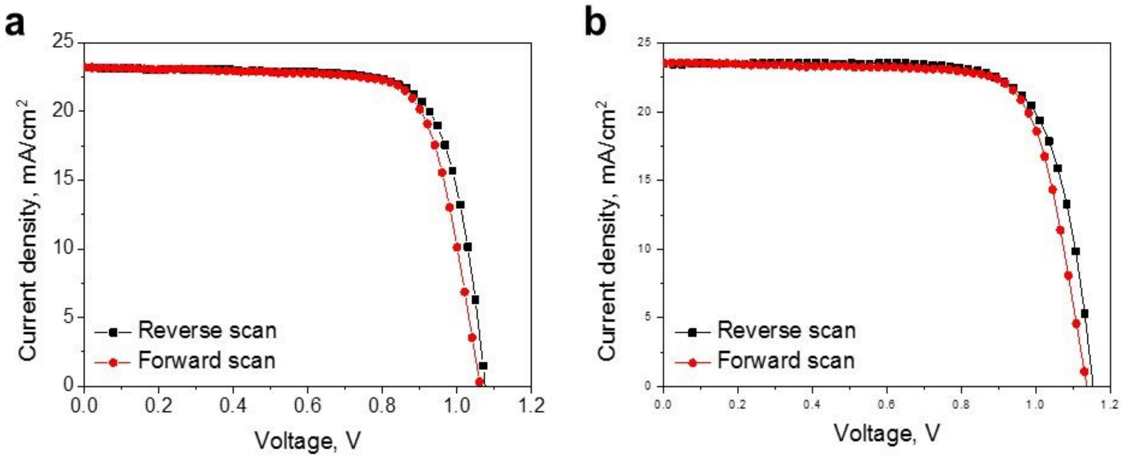

Figure S16. Representative forward and reverse scans of the champion devices fabricated with $Cs_{0.05}(FA_{0.85}MA_{0.15})_{0.95}Pb(I_{0.85}Br_{0.15})_3$ perovskite light absorber in combination with the (a) non-Pb-capped TiO_2 and (b) Pb-capped (Pb13) TiO_2 ETLs. The difference between forward and reverse scans was around 1.5% for PSCs with TiO_2 ETLs with and without PbO capping.

Current density-voltage characteristics of PSCs with triple cation-based light absorbers.

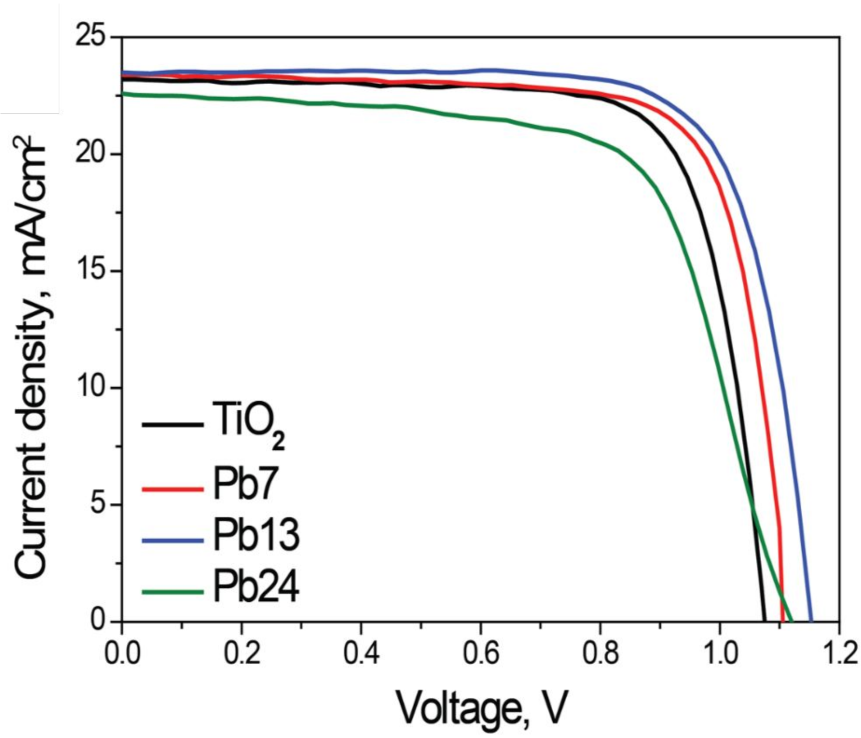

Figure S17. Current density–voltage characteristics for the best control devices based on CsFAMA light absorbers with and without PbO treated ETLs.

Current-voltage curves of PSCs in dark condition and under illumination.

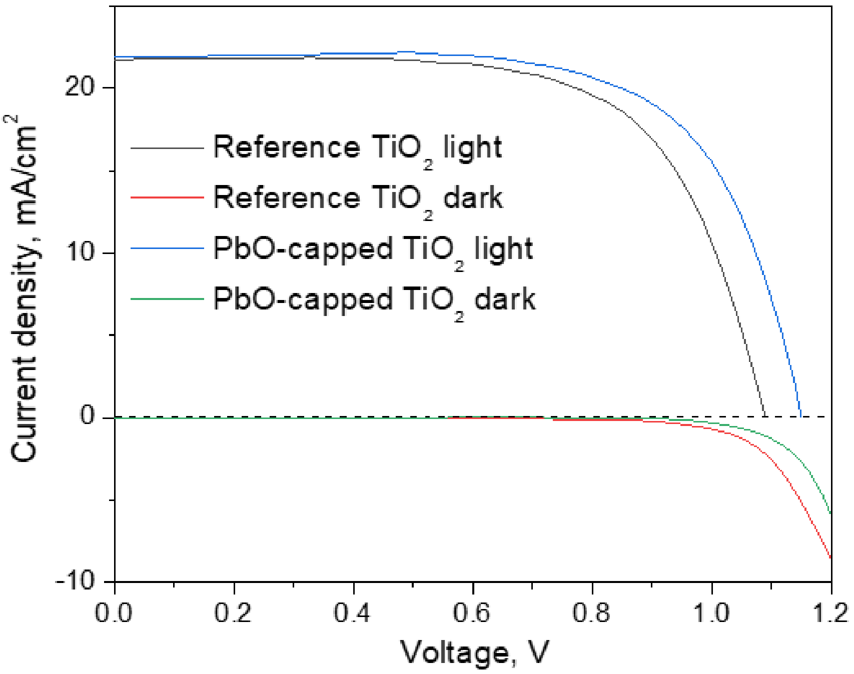

Figure S18. Current-voltage curves of PSCs with and without PbO capping recorded in dark condition and under illumination.

Performance of the PSCs with Pb-capped $SrTiO_3$ and ZnO ETLs. The current-voltage (J-V) curves of champion devices fabricated with $Cs_{0.05}(FA_{0.85}MA_{0.15})_{0.95}Pb(I_{0.85}Br_{0.15})_3$ perovskite light absorber and ZnO and $SrTiO_3$ ETLs with and without PbO capping are shown in Fig. S19. In principle, the PSC efficiency could be attributed to the thickness of an ETL layer and the large particle size in the ETL. However, the thicknesses and particle sizes are determined to be the same for the devices with different Pb capping levels, thus indicating that the increased PSC performance is attributed to the effect of Pb-capping leading to the better interface with perovskite, similar to the TiO_2 ETL case. Furthermore, the increase in energy conversion efficiency of a device is found to be resulting from the enhancements in V_{oc} and FF parameters. These clarify that the presence of Pb at the surface of an ETL plays a positive role in establishing the better interface with a perovskite light absorber.

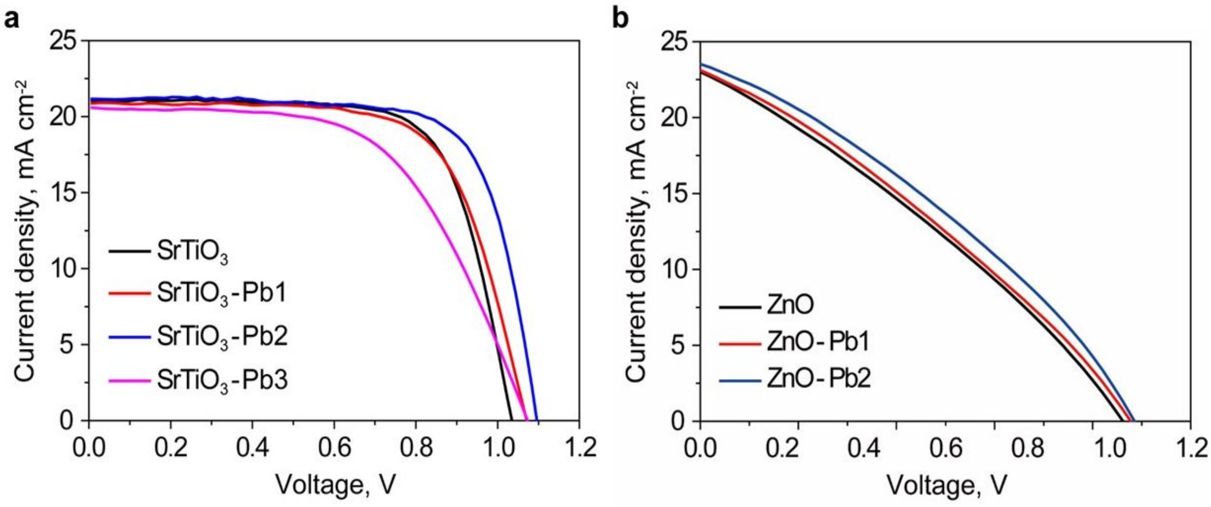

Figure S19. Performance of the PSCs with Pb-capped $SrTiO_3$ and ZnO ETLs. (a) The J–V curves and (b) short circuit current curves for PSCs fabricated $SrTiO_3$ and ZnO ETLs with and without PbO cappings.

Performance of the PSCs with Sn-capped TiO_2 ETLs. The current-voltage (J-V) curves of champion devices fabricated with $Cs_{0.05}(FA_{0.85}MA_{0.15})_{0.95}Pb(I_{0.85}Br_{0.15})_3$ perovskite light absorber and TiO_2 ETLs with and without SnO_2 capping are shown in Fig. S20. We find that the performance of the PSCs with Sn capping is similar regardless of the amount of Sn deposited. Also, it is determined that the FF and V_{oc} parameters of these devices are not improved with Sn capping. Furthermore, the first-principle calculations confirm that the Sn capping at TiO_2 layer does not lead to significant change in the structure of TiO_2/perovskite interface and does not lead to the improvement of energy conversion efficiency.

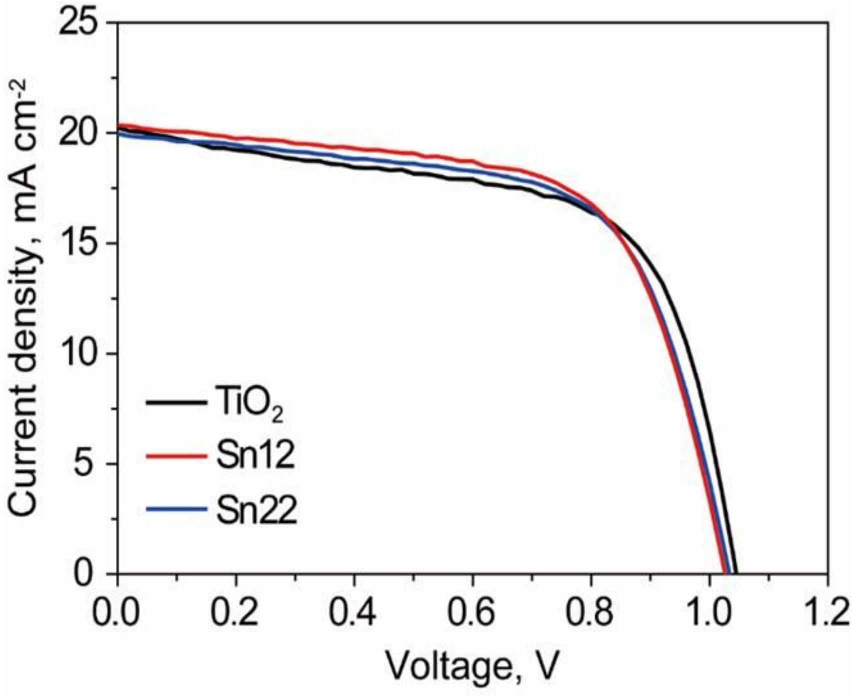

Figure S20. J–V curves of PSCs fabricated with TiO_2 ETLs with and without SnO_2 capping.

Section 3. Supplementary tables

Photovoltaic parameters of champion devices fabricated with TiO_2 ETLs with and without PbO capping. The energy conversion parameters of champion devices fabricated with $Cs_{0.05}(FA_{0.85}MA_{0.15})_{0.95}Pb(I_{0.85}Br_{0.15})_3$ perovskite light absorber are listed in Table S1. It shows that the high PSC efficiency upon Pb capping is obtained for cells based on Pb13 TiO_2 layers. Upon increasing the Pb capping level, we find that the V_{oc} and FF parameters of devices increase, while the photocurrents remain almost at the same level. With the optimum capping of a TiO_2 layer with PbO, the PSC efficiency is also observed to be significantly enhanced compared to the sample based on a TiO_2 ETL without PbO capping. Moreover, we observed the similar trend of V_{oc} and FF parameters in PSCs with the $MAPbI_3$ and various ETLs.

ETL	J_{sc} (mA/cm^2)	V_{oc} (V)	FF (%)	Efficiency (%)
TiO_2	23.2	1.09	74	18.7
Pb7	23.4	1.12	75	19.7
Pb13	23.5	1.15	78	21.2
Pb24	22.6	1.10	68	16.7

Table S1. Photovoltaic parameters of champion devices fabricated with CsFAMA perovskite and TiO_2 ETLs with and without PbO capping.

ETL	J_{sc} (mA/cm^2)	V_{oc} (V)	FF (%)	Efficiency (%)
TiO_2	20.3	1.07	67	14.6
Pb7	19.7	1.09	70	15.1
Pb13	20.3	1.12	73	16.5
Pb24	18.9	1.13	66	14.1

Table S2. Photovoltaic parameters of champion devices fabricated with $MAPbI_3$ perovskite and TiO_2 ETLs with and without PbO capping.